PAPER

Anisotropic interfacial properties of monolayer GeSe—metal contacts

IOP Publishing Semiconductor Science and Technology
Semicond. Sci. Technol. **34** (2019) 095021 (12pp) https://doi.org/10.1088/1361-6641/ab37cc

Anisotropic interfacial properties of monolayer GeSe—metal contacts

Ying Guo[1,2,6], Feng Pan[2], Yajie Ren[2], Yangyang Wang[5], Binbin Yao[2], Gaoyang Zhao[1,6] and Jing Lu[3,4,6]

[1] School of Materials Science and Engineering, Xi'an University of Technology, Xi'an, 710048, People's Republic of China
[2] School of Physics and Telecommunication Engineering, Shaanxi Key Laboratory of Catalysis, Shaanxi University of Technology, Hanzhong 723001, People's Republic of China
[3] State Key Laboratory of Mesoscopic Physics and Department of Physics, Peking University, Beijing 100871, People's Republic of China
[4] Collaborative Innovation Center of Quantum Matter, Beijing 100871, People's Republic of China
[5] Nanophotonics and Optoelectronics Research Center, Qian Xuesen Laboratory of Space Technology, China Academy of Space Technology, Beijing 100094, People's Republic of China

E-mail: guosophia@163.com, zhaogy@xaut.edu.cn and jinglu@pku.edu.cn

Received 1 May 2019, revised 2 July 2019
Accepted for publication 1 August 2019
Published 27 August 2019

Abstract

Monolayer germanium selenide (ML GeSe) has been experimentally fabricated recently. It is a new member of the two-dimensional (2D) semiconductor material group and shares a similar pucker structure, direct band gap, anisotropy, and high carrier mobility with isoelectronic ML phosphorene. Additionally, it had an advantage over phosphorene in that it is intensely ambiently stable and thus more suitable for a channel material for next-generation high-performance transistors. We systematically research the contact properties between ML GeSe and electrodes (Cu, Ag, Ti, Au, Pd, Pt, graphene and graphene-Cu) in a transistor configuration by using first-principle and quantum transport calculations. ML GeSe field effect transistors (FETs) have strong Fermi level pinning and anisotropic Schottky contacts in the lateral interface. Graphene electrodes have a dramatic lateral *p*-type (quasi-*p*-type) ohmic contact in the *b* (*a*)-axis direction of ML GeSe FETs, and graphene-Cu hybrid electrodes have a quasi-*p*-type ohmic contact in the *a*-axis direction. Hence, high performance can be achieved in ML GeSe FETs with graphene electrodes or via the insertion of graphene between the ML GeSe and a Cu electrode.

Supplementary material for this article is available online

Keywords: Ohmic contact, monolayer GeSe, first-principle theory, quantum transport simulation

(Some figures may appear in colour only in the online journal)

1. Introduction

Two-dimensional (2D) semiconductors, such as transition-metal dichalcogenides (TMDs), phosphorene, bismuthene, tellurene, and monolayer (ML) InSe have been extensively investigated [1–14] for their unique electronic and optical properties. Compared with bulk semiconductor materials, 2D semiconductors can be more effectively controlled by the gate due to their atomic scale thickness and they have better carrier transportation ability owing to the absence of dangling bonds and atomic scale uniform thickness. Hence, they are hopeful candidate channel materials for future transistors [1, 15–17]. Among 2D semiconductors, puckered phosphorene is distinguished by its high carrier mobility ($\sim$1000 $cm^2 V^{-1} s^{-1}$), apparent anisotropy and excellent device performance in the sub 10 nm region [18, 19]. Unfortunately, phosphorene is unstable in ambient air, which greatly restricts the practicable device application [3, 13].

Binary ML monolayer IV–VI chalcogenides (SnS, SnSe, GeS and GeSe), another new 2D family material with proper

[6] Authors to whom any correspondence should be addressed.

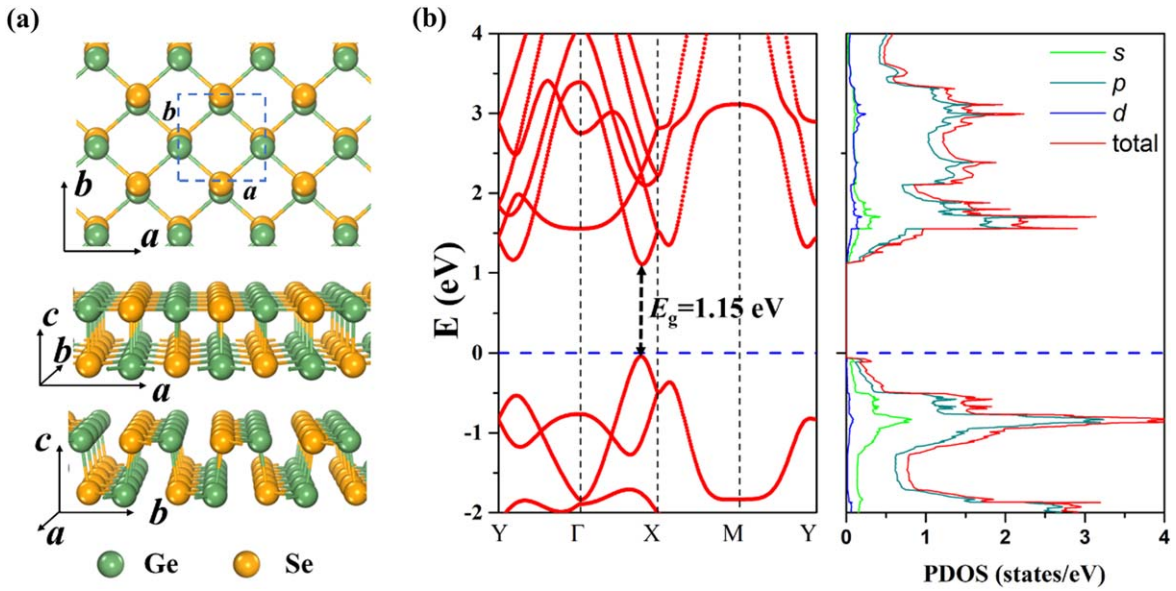

Figure 1. (a) View of free-standing GeSe. The rectangle shows the unit cell. (b) Band structure and partial density of states (PDOS) of free-standing GeSe.

band gap (1.1–1.5 eV) [20–23], are made up of earth-abundant and low-toxic elements. They have a puckered structure and anisotropic properties similar to isoelectronic phosphorene [24]. Remarkably, they are very stable in ambient air [25, 26]. Among binary IV-VI chalcogenides, germanium selenide (GeSe) is the only one that has a direct band gap of 1.16 ± 0.13 eV [27, 28]. The close located direct and indirect band gaps of GeSe are in the range of 1.1–1.2 eV, which overlap pretty well with the solar spectrum [28–30]. Therefore, 2D GeSe shows attractive optical properties of photoelectronic application and high optical absorption [27, 31–34]. Actually, solar cells and photodetectors based on multilayer GeSe have been fabricated with Au electrodes and SiO_2/Si substrates [28, 35]. Moreover, thin-film GeSe is easily fabricated by a rapid thermal sublimation, and ML GeSe is predicted to have a high carrier mobility ($\sim$4000 $cm^2\ V^{-1}\ s^{-1}$) [36], which is comparable with that of phosphorene. High ambient stability and carrier mobility render ML GeSe a more promising channel material for next-generation high-performance transistors compared with ambient unstable phosphorene. In an actual 2D optoelectronic or electronic device, ML GeSe often needs contact with metal electrodes to inject proper carriers because of the lack of an effective substitutional doping scheme. A Schottky barrier always exists in the interface of the 2D semiconductor-metal devices, and it induces an extra contact resistance, which always significantly reduces the performance of devices. Therefore, finding a low-resistance interface with a proper metal electrode is essential to maximize device performance. The interfacial properties of 2D materials, such as phosphorene (1–3 layers), arsenene, bismuthene, TMDs tellurene, and ML InSe [8–10, 14, 37–41] contacts with metal electrodes have been intensively investigated. There is a need to simulate the interfacial properties of ML GeSe-metal contacts for the prediction of suitable ML GeSe devices.

In this paper, we first comprehensively study the vertical and lateral interface of ML GeSe (hereafter, 'GeSe' represents 'ML GeSe') field effect transistors (FETs) with the bulk metal electrodes (Cu, Ag, Ti, Pd, Au, Pt, graphene, and graphene-Cu) by using density functional theory (DFT) and *ab initio* quantum transport simulation. The GeSe FETs have good ohmic contact in the vertical interface because GeSe undergoes a metallization and has anisotropic lateral Schottky contacts. Along the *a*-axis, *n*-type Schottky barriers of 0.45 (Ag) and 0.51(Pt) eV are formed, while *p*-type Schottky barriers of 0.22(Au), 0.31(Cu), 0.37(Ti), and 0.50(Pd) eV, respectively, are formed. Along the *b* axis, *n*-type Schottky barriers of 0.30(Ag) and 0.53(Cu) eV are formed, while *p*-type Schottky barriers of 0.40(Pt), 0.41(Ti), 0.42(Pd) and 0.54 (Au) eV, are formed. Strong Fermi level pinning (pinning factor 0.14) is noted in the *b*-axis of GeSe FETs. It is interesting that in the lateral interface of the *b* (*a*)-axis and *a*-axis, a p-type (quasi-p-type) and quasi-p-type ohmic contact are formed when graphene is the electrode and with a graphene insert between GeSe and Cu. Hence, high performance GeSe FETs can be made with graphene electrodes or via insertion of graphene between the GeSe and a Cu electrode.

2. Computational details

The lattice parameters ($a = 3.99$ Å, $b = 4.26$ Å (shown in figure 1)) of GeSe are in good agreement with the previous results [20, 21, 28, 42]. Six common metals (Cu, Ag, Ti, Au, Pd, and Pt) covered a wide work function (3.29 $\sim$ 5.36 eV) are used as electrodes. We adapt 1×3 Ag(110)/Au(110)/Pd (110) to 1×2 GeSe supercell and 1×3 Pt(110)/$3 \times \sqrt{3}$ Cu (111)/$\sqrt{3} \times 1$ Ti (111) to 2×1 GeSe supercell. Mismatch degrees between the GeSe and metal electrodes are 1.23 $\sim$ 3.46% (as listed in table 1). Convergence tests in the preceding studies [41] show that a six-metal-layers model is

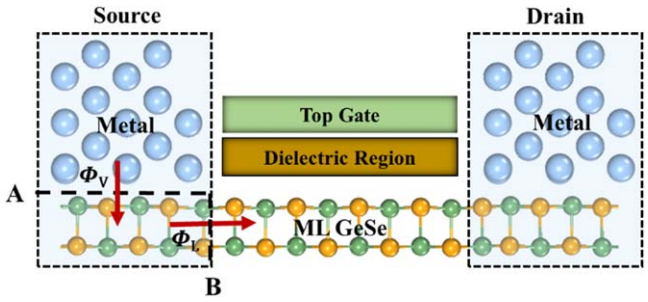

Figure 2. The structural diagram of GeSe FETs. A/B is the vertical/lateral interface where Schottky barriers (Φ_V/Φ_L) may exist. The red arrows denote the pathway of electron or hole carriers from the electrode regions to the channel GeSe.

enough to calculate the bulk metal electrode, and the atomic positions of bottom layer is kept fixed and the other five layers are free. In our periodic model, to avoid pseudo interaction, the vacuum space is adopted at least 15 Å in the z direction.

The plane-wave basis set and the projector-augmented-wave (PAW) pseudopotential DFT calculation was used for the relaxation energy calculation in the Vienna *ab initio* simulation package (VASP) [43, 44]. The van der Waals correction is simulated by the DFT-D2 method of Grimme [45, 46], and in the z-direction dipole correction is simulated [47]. The convergence standard of energy per atom is less-than 1×10^{-6} eV. The atomic positions are fully optimized unless the maximum force per atom is less-than 0.001 eV Å^{-1}. In geometry optimizations (energy band calculations), the cutoff energy is 400 (500) eV, and the k-points are sampled as $9 \times 9 \times 1$ ($24 \times 24 \times 1$) in the Brillouin integration. After examining the stabilized structures of the ML GeSe-Ag interface optimized by the VASP and ATK codes, it can be seen that the methods are quite similar (figure S1 is available online at stacks.iop.org/SST/34/095021/mmedia). The Δ, d_{min}, and d_0 values of the ML GeSe-Ag interfacial system are 2.67/2.69, 2.62/2.46, and 2.29/2.30 Å calculated by VASP/ATK, respectively.

The two-probe model is used to simulate the GeSe FETs (figure 2). This kind of top-contact configuration has two types of interface: vertical interface (A: between the metal electrodes and GeSe in source/drain regions) and lateral interface (B: between the GeSe electrode and channel). Take about 5 nm intrinsic GeSe as the channel region, and two electrode regions are semi-infinite with GeSe/metal compound systems. In the electrode region, the Neumann and Dirichlet boundary conditions are used, that ensure the electron/hole neutrality. The quantum transport is simulated by the DFT coupled with the non-equilibrium Green's function (NEGF) in the ATK 2018 package. The k-points are sampled as $19 \times 1 \times 129$ ($k_x \times k_y \times k_z$) ($19 \times 1 \times 129$) in the channel (electrodes) region. The basis set is the double-ζ polarized (DZP) with the FHI pseudopotentials and the temperature is 300 K.

The transmission coefficient $T(E)$ is an average of $T(kx,\ E)$ over 129 k_x-points, and k_x is a vector vertical to the transport direction. $T(k_x, E)$ is expressed as (1) when energy E is given:

$$T(k_x, E) = T_r(G^r(k_x, E)\Gamma_L(k_x, E)G^a(k_x, E)\Gamma_R(k_x, E)) \quad (1)$$

where $G^r(k_x, E)(G^a(k_x, E))$ is the retarded (advanced) Green function, $\Gamma_{L(R)}(k_x, E)$ indicate the level broadening and scattering region by left/right electrode and is expressed as:

$$\Gamma_{L(R)}(k_x, E) = i(\Sigma^r{}_{L(R)}(k_x, E) - \Sigma^a{}_{L(R)}(k_x, E)) \quad (2)$$

$\Sigma_{L(R)}(E)$ is the electrode self-energies.

The generalized gradient approximation (GGA) with the Perdew-Burke-Ernzerhof (PBE) scheme to the exchange-correlation functional is adopted. Because the electron-electron interactions in the 2D semiconductor channel region are greatly screened by doping carriers from the electrode, single electron approximation (DFT-PBE) becomes a good approximation to describe the electronic structure of the FETs device. For example, the experimental and simulated (at the DFT-PBE level) transport gaps (in terms of the local device density of states) of ML, bilayer, and trilayer black phosphorene FETs with Ni electrode are 1.00/0.79, 0.71/0.81, and 0.61/0.68 eV, respectively [10, 48, 49]. Therefore, we used the DFT-PBE to depict the FET device. The simulated p-type ohmic or quasi-ohmic contact for ML and BL WSe_2 with Pt electrode is well consistent with experimental results of a dual-gated WSe_2 FET with Pt electrode [11, 50]. The MoS_2 FET with Au and Pt electrodes also have the same results in

Table 1. Simulated properties of the GeSe-metal compound systems. $\bar{\varepsilon}$ is the lattice mismatch between the GeSe and metals, d_0 the vertical distance from the bottom GeSe atom layer to the topmost metal atom layer, d_{min} the minimum distance of atom to atom from GeSe to the metals. Δ is the vertical distance from the topmost layer to the bottom atom layer of GeSe in contact with metal electrodes. E_b is the binding energy (each GeSe atom) needed to remove GeSe layer from the metal electrodes. W_M and W are the work functions of metal electrode and the GeSe-metal compound systems. $\Phi^e_{W,L}$ ($\Phi^h_{W,L}$) is electron (hole) Schottky barrier height (SBH) using the work function approximation. $\Phi^{e,a}_{T,L}$ and $\Phi^{e,b}_{T,L}$ ($\Phi^{h,a}_{T,L}$ and $\Phi^{h,b}_{T,L}$) are the electron (hole) SBH using the transport simulation in lateral a-axis and b axis, respectively. $E_g^{L,a}$ and $E_g^{L,b}$ are the transport gap in lateral a axis and b axis. The lattice constant of GeSe is $a = 4.26$/$b = 3.99$ Å, and the work function is 4.45 eV.

Metal	Cu	Ag	Au	Pd	Pt	Ti
$\bar{\varepsilon}$ (%)	2.61	1.35	1.23	1.93	1.35	3.46
d_0 (Å)	2.17	2.29	2.33	1.08	0.90	−0.54
d_{min} (Å)	2.53	2.62	2.54	2.42	2.42	2.49
Δ (Å)	2.82	2.67	2.81	4.08	3.66	4.75
E_b (eV/GeSe)	1.70	0.20	1.31	4.21	3.97	5.70
W_M (eV)	4.69	4.18	4.98	4.77	5.36	3.29
W (eV)	4.39	4.05	4.38	4.69	4.63	3.68
$\Phi^e_{W,L}$ (eV)	0.51	0.17	0.50	0.81	0.75	−0.20
$\Phi^h_{W,L}$ (eV)	0.64	0.98	0.65	0.34	0.40	1.35
$\Phi^{e,a}_{T,L}$ (eV)	0.86	0.45	0.85	0.74	0.51	0.78
$\Phi^{h,a}_{T,L}$ (eV)	0.31	0.71	0.22	0.50	0.71	0.37
$\Phi^{e,b}_{T,L}$ (eV)	0.53	0.30	0.61	0.62	0.71	0.47
$\Phi^{h,b}_{T,L}$ (eV)	0.67	0.83	0.54	0.42	0.40	0.41
$E_g^{T,a}$(eV)	1.17	1.16	1.07	1.24	1.12	1.15
$E_g^{T,b}$(eV)	1.10	1.13	1.15	1.04	1.11	0.88

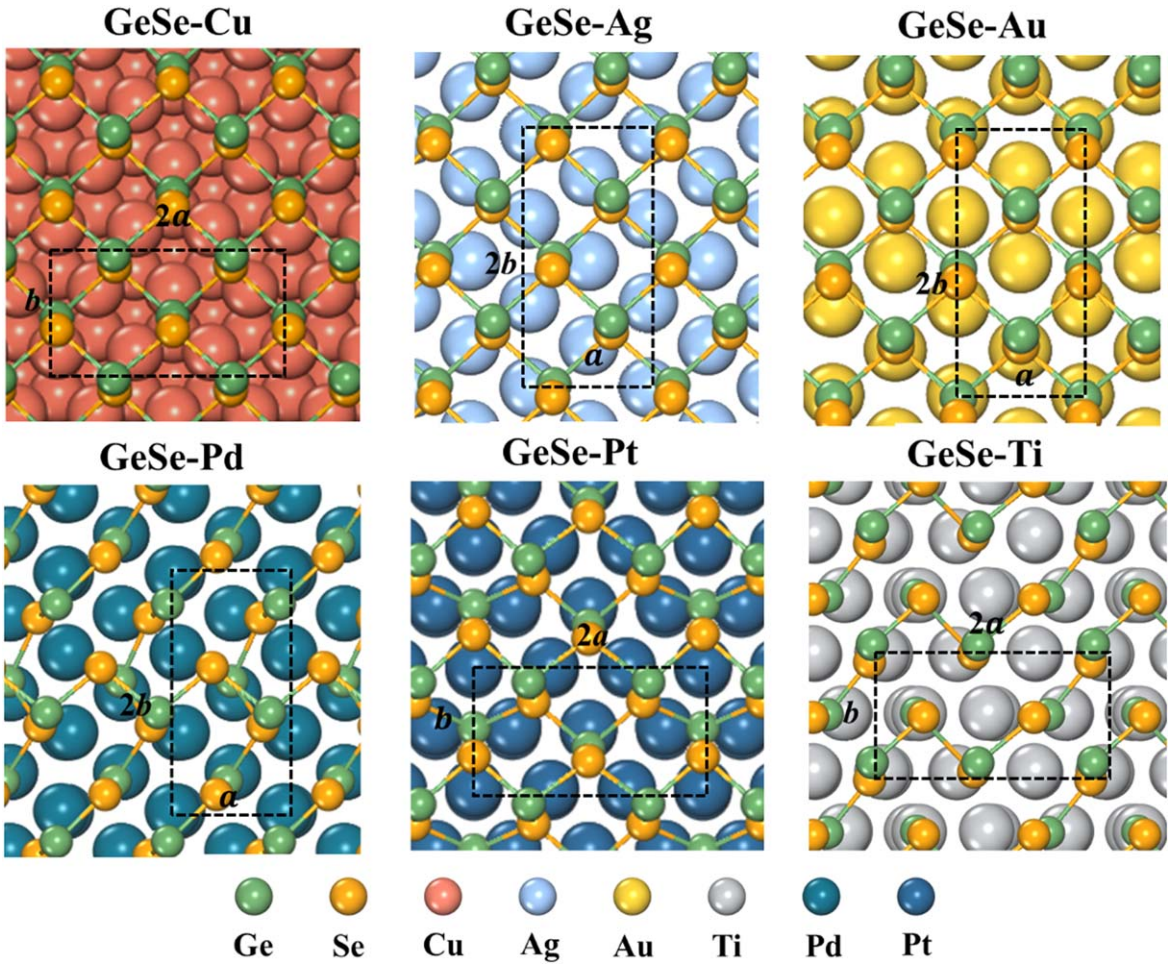

Figure 3. Top views of the stable configuration for (1 × 2) GeSe on the (1 × 3) Ag (110)/Au (110)/Pd (110), (2 × 1) GeSe on the (1 × 3) Pt(110)/(3 × $\sqrt{3}$) Cu (111)/($\sqrt{3}$ × 1)Ti (111). The black rectangles represent the unit cells.

simulations and experimentations. The Pt electrode has an *n*-type Schottky barrier (0.28 eV) by the quantum transport simulation, which is accord with the results (electron SBH: 0.14–0.26 eV) of the experiments [51, 52]. The Au electrode has an *n*-type Schottky barrier (0.20 eV) by the simulation, which is consistent with the experimental value of 0.06/0.13/0.32 eV [52–54].

3. Results and discussion

3.1. Vertical interface properties of the GeSe and metal contact

Three kinds of stacking pattern with high symmetry are considered as the initial configurations. After relaxation, the most stable GeSe/metal systems are shown in figures 3 and 4. Puckled GeSe has a tiny change on the Cu, Ag, and Au electrodes, while has a seriously destruction on the Ti, Pd, and Pt electrodes. As shown in table 1, the binding energy E_b of the GeSe/metal defined as:

$$E_b = (E_{GeSe} + E_{metal} - E_{GeSe/metal})/N_{GeSe} \quad (3)$$

where E_{GeSe} is energy of GeSe, E_{metal} is energy of pure metal electrode and $E_{GeSe/metal}$ is the energy of composite system per supercell. N_{GeSe} is the number of GeSe atoms per supercell.

The E_b of GeSe/metals composite systems increased in the order of Ag (0.20) < Au (1.31) < Cu (1.70) < Pt (3.97) < Pd (4.21) < Ti (5.70 eV). We can qualitatively divide the interactions of GeSe/metal compound systems into a weak and a strong chemical bonding. The weak chemical bonding is formed between GeSe and Ag/Au/Cu with larger interfacial distance d_0 (the vertical distance from the GeSe the metal atom layer) (2.29(Ag), 2.33(Au) and 2.17(Cu) Å) and larger atom-to-atom distance d_{min} (2.62 (Ag), 2.54(Au) and 2.53(Cu) Å). The d_{min} is the minimum distance of atom-to-atom from metals to the GeSe. The vertical interface of GeSe and Pd/Pt electrodes has a strong chemical bonding with smaller d_0 (1.08/0.90 Å) and d_{min} (2.42/2.42 Å). The largest E_b (5.70 eV) is GeSe/Ti compound system with smaller d_{min} (2.49 Å) and negative d_0 (−0.54 Å) explain the especially large morphing of GeSe on Ti, and a new compound system is formed.

The numbers of unpaired electrons lead to the different bond strength of GeSe/metal compound systems. The outermost orbital of IB-group (Au($5d^{10}6s^1$), Ag($4d^{10}5s^1$), and Cu($3d^{10}s^1$)) have only one unpaired electron, when they as the solid-state electrodes contact with GeSe form one covalent

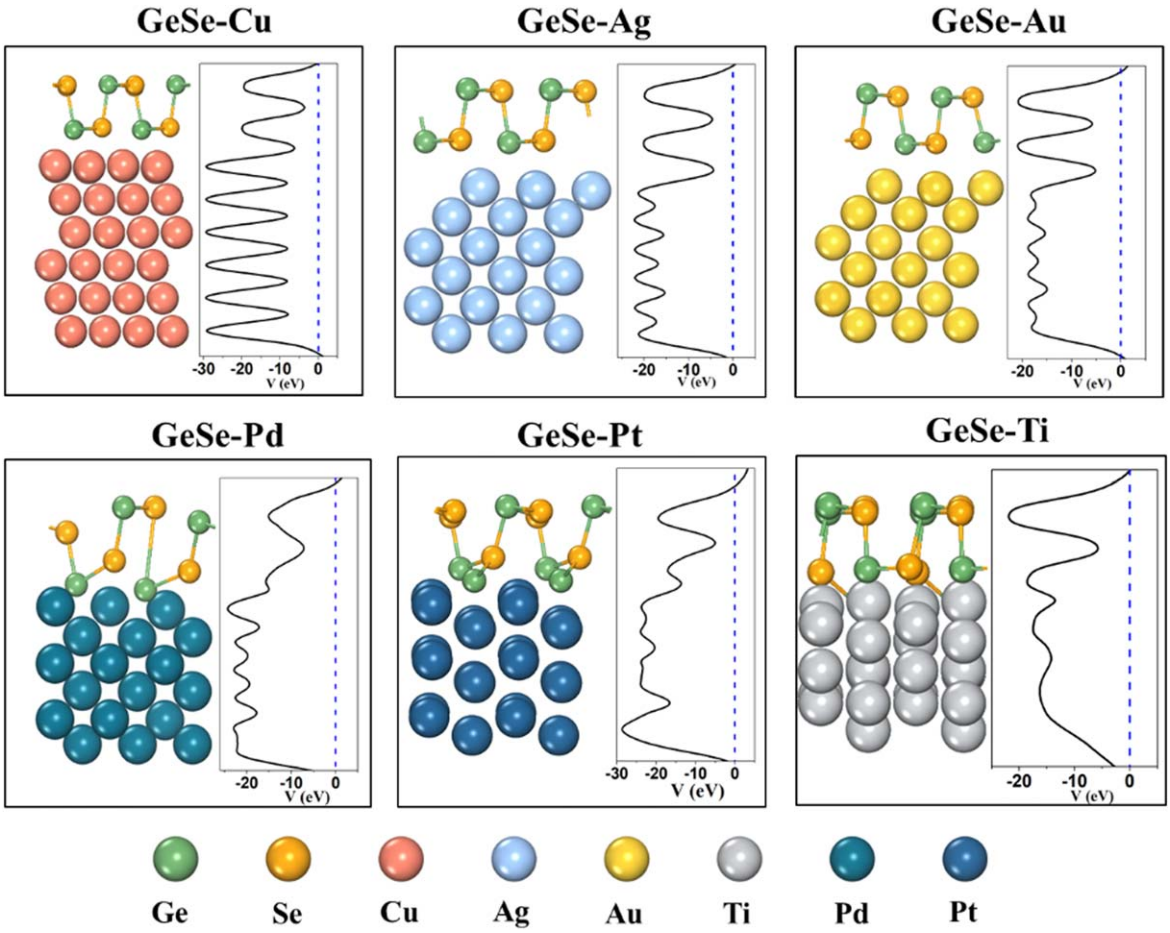

Figure 4. The stable configurations (side view) and average electrostatic potentials (AEP) of GeSe on the Cu, Ag, Au, Ti, Pd, and Pt electrodes, respectively. The Fermi level is at zero energy.

bond, corresponding to the weak E_b. Pt atom ($5d^9 6s^1$) and Ti atom ($3d^2 4s^2$) shape two and four covalent bonds with GeSe because of having two and four unpaired electrons. The n*d* and (n + 1) *s* shells redistribute electrons when transition metal atoms form a solid. Although Pd atom ($4d^{10}$) has zero unpaired electron, in fact, Pd has an electronic distribution similar to that of Pt. Therefore, Pd shape two covalent bonds with GeSe, corresponding to the strong E_b.

Figure 4 also shows the average electrostatic potentials (AEP) of GeSe/metal contacts. In the vertical interface, the tunneling barrier ΔV is described as the AEP over the Fermi level (E_f) between GeSe and the metals. There is no AEP over the E_f in the interface, and as a result, no tunneling barrier arises in the vertical interface of GeSe/metal contacts. The band structures of GeSe/metal contacts are shown in figure 5. Compared with the free-standing GeSe, the band structure of GeSe come from compound systems are all severely destroyed, suggesting a covalent in the vertical interface. The hybridization levels of GeSe in contact with the Pd, Pt, and Ti electrodes are stronger than those of the Cu, Ag, and Au electrodes. In addition, the Fermi level pass through the band of GeSe/metal contacts, suggesting that GeSe has undergone metallization.

Figure 6 shows the partial density of states (PDOS) of the GeSe/metal contact, and the band gap disappears, confirming the metallization of GeSe supported by the metal electrodes. Therefore, GeSe and metal electrodes form an ohmic contact in the vertical interface. Figure S2 shows the total electron distribution, and the accumulation of electrons is obvious in the vertical interface, suggesting a covalent bond.

3.2. Lateral interface and quantum transport properties of the GeSe FETs

As shown in figure 2, if the Schottky barriers exist in the interface of semiconductor and electrode of FETs, they will affect the performance of FETs because of depressing the electron/hole transport. In GeSe FETs, the GeSe/metal contacts of source/drain region are metallization, indicting Φ_V (the vertical Schottky barriers) is zero, and the lateral interface may be Schottky barriers contact and Φ_L (the lateral Schottky barriers) is not zero.

We will get Φ_L by two methods: the work function approximation (WFA) and the quantum transport simulation. In the popular WFA method, the $\Phi_{W,L}^{e(h)}$ (electron/hole SBH) of GeSe FETs is defined by the difference between the Fermi level values of the metallized GeSe and CBM (VBM) of the channel GeSe. The Ag/Au/Cu electrodes have *n*-type Schottky barriers ($\Phi_{W,L}^{e}$) of 0.17, 0.50, and 0.51 eV, respectively. The Pd and Pt electrodes have *p*-type Schottky barriers

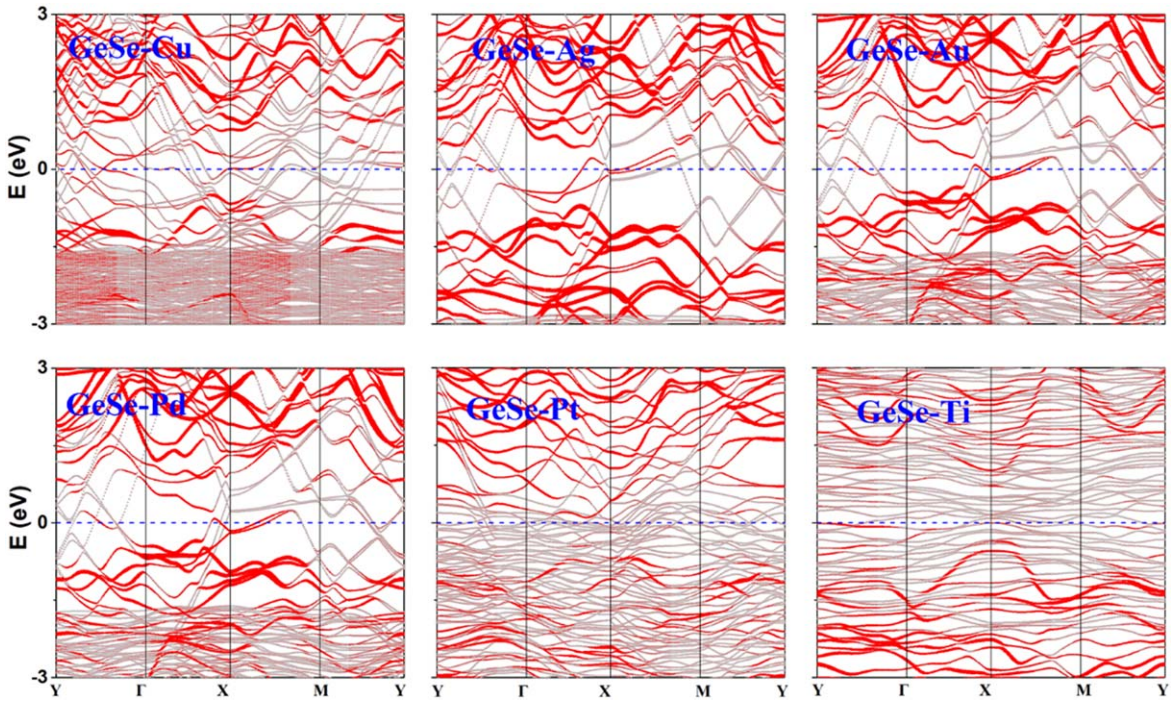

Figure 5. Energy band graph of GeSe with Cu, Ag, Au, Pd, Pt, and Ti electrodes, respectively. Gray dots correspond to the GeSe-metal compound systems. Red dots correspond to the states with valid contribution from GeSe, and the radii of the dots are proportional to the weight.

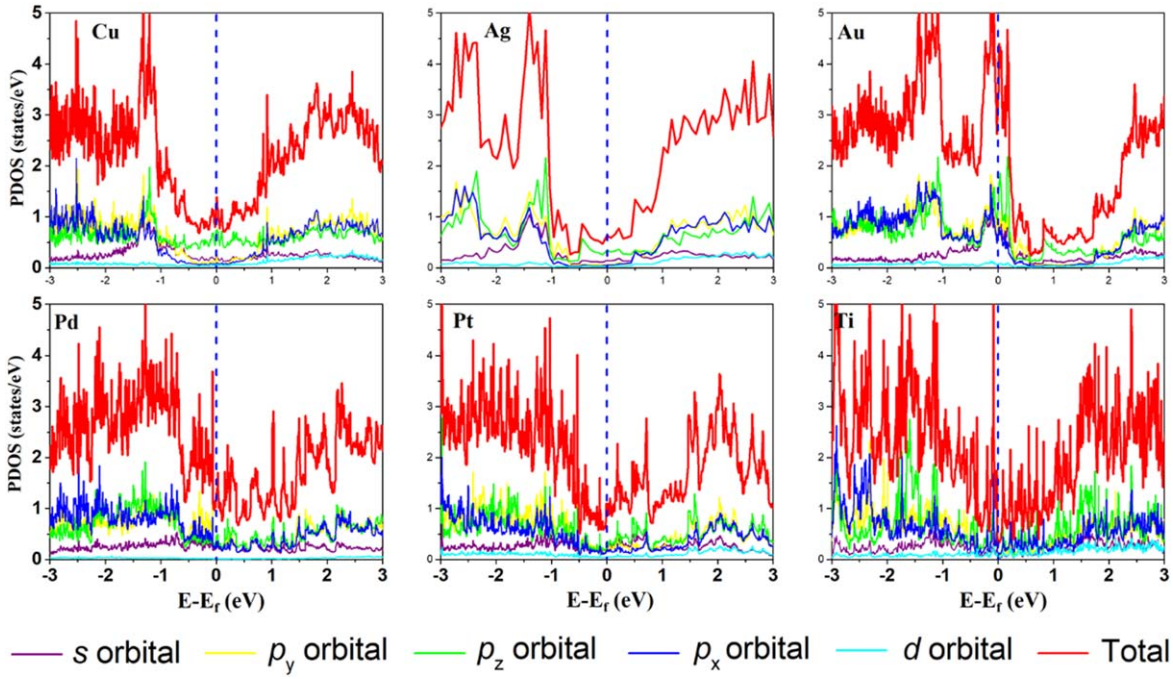

Figure 6. Partial density of states (PDOS) of GeSe on the Cu, Ag, Au, Pd, Pt, and Ti electrodes.

($\Phi^{h}_{W,L}$) of 0.34 and 0.40 eV, respectively. The Ti electrode has *n*-type ohmic contact (list in table 1). The interaction between the channel and electrode regions is overlooked by WFA, thus a more reliable method, quantum transport simulation, should be used.

The quantum transport method define the $\Phi^{e(h)}_{T,L}$ (electron/hole SBH) of GeSe FETs by the difference between the Fermi level and CBM (VBM) of the channel at the lateral interface, that can be evaluated by local density of states (LDOS) of GeSe FETs. The LDOS can offer more details of the vertical and lateral interface, such as metal-induced gap states (MIGS) (the new electronic states in the band gap of semiconductor that comes from metal), and thus the contact type and values of SBH calculated by the LDOS are more precise. The LDOS

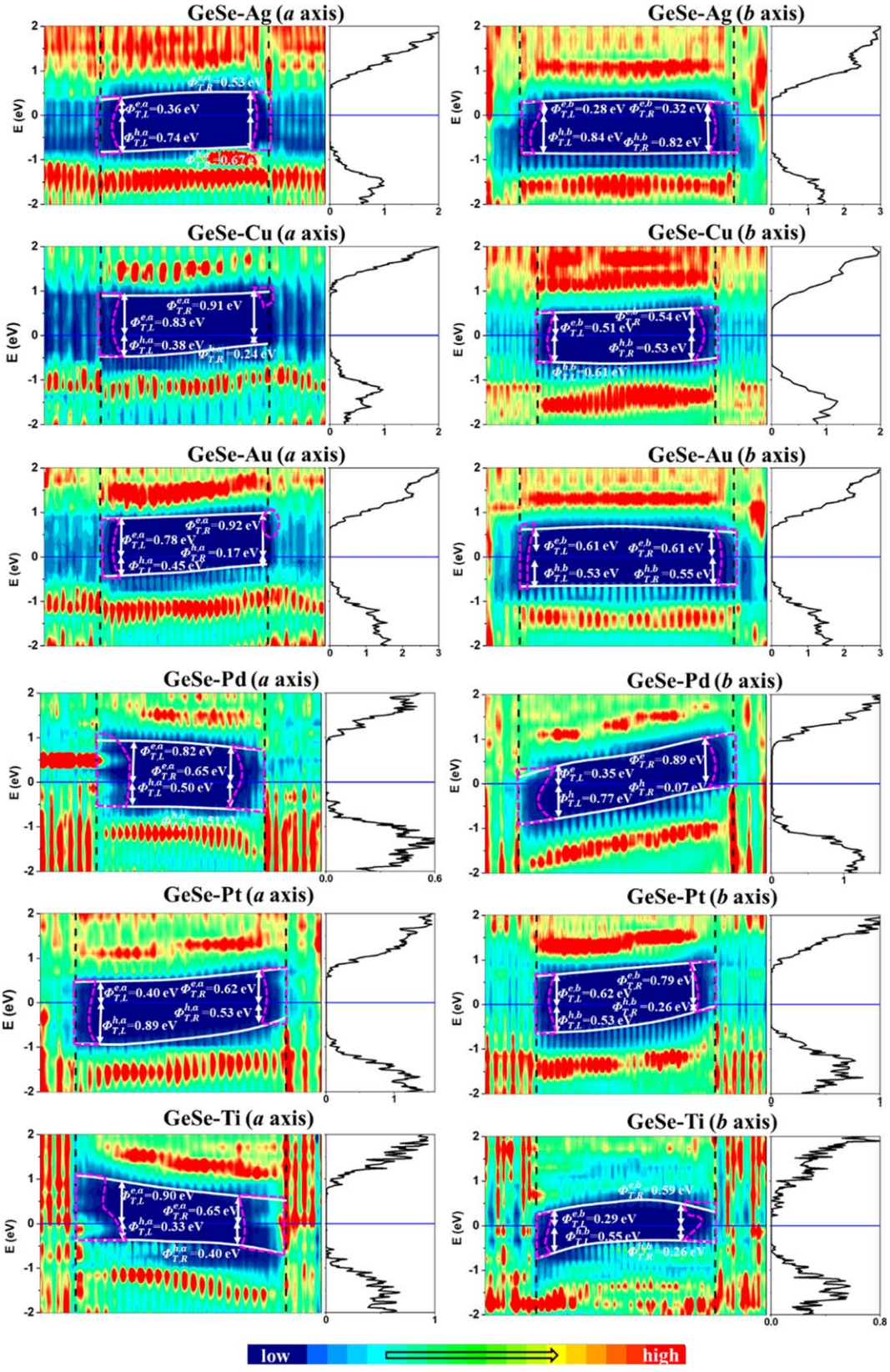

Figure 7. The color coding of local density of states (LDOS) projected on the GeSe and transmission spectrum (TS) of the GeSe FET with metal electrodes (Ag, Cu, Au, Pd, Pt, and Ti) under the 0-bias and 0-gate voltage, and the channel length is about 5 nm. Magenta lines surrounded area are the region with MIGS. The Fermi level is at zero energy. The upright black dashed lines are the interface of source (drain) and the channel. The conduction band and valence band profiles along the channel are given in white lines.

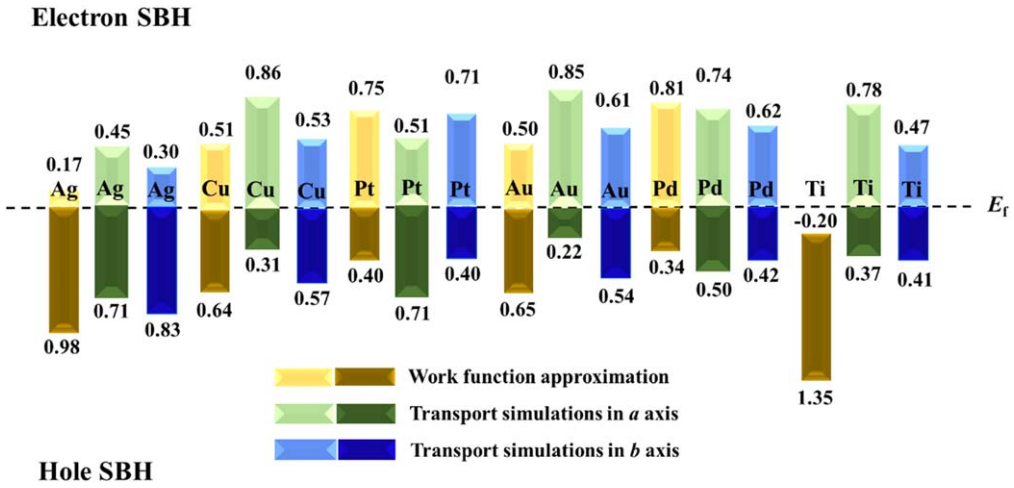

Figure 8. Comparison of the lateral electron and hole SBHs of the GeSe on Ti, Cu, Ag, Au, Pd, and Pt. The light (deep) yellow, green and blue rectangle present the electron (hole) SBH using the work function approximation (WFA) and the transport simulations in *a* and *b* axis, respectively.

color coding of GeSe FETs projected on the GeSe and transmission spectrum (TS) of the GeSe FETs under the zero-bias and zero-gate voltage are shown in figure 7.

The puckered GeSe gives rise to anisotropy in the transport properties, and so we take into account two axes (*a* and *b* directions as shown in figure 1(a)) of the GeSe FETs in the quantum transport simulation. Considering the asymmetrical FETs, the values of *n*(*p*)-type Schottky barriers ($\Phi_L^{e(h)}$) are the average of the left and right Schottky barriers ($\Phi_{L,L}^{e(h)}$ and $\Phi_{L,R}^{e(h)}$) at lateral interface [10, 48, 49]. Along *a*-axis, the Ag/Pt electrodes have *n*-type Schottky barriers ($\Phi_L^{e,a}$) of 0.45/0.51 eV, while the Au/Cu/Ti/Pd electrodes have *p*-type Schottky barriers ($\Phi_L^{h,a}$) of 0.22/0.31/0.37/0.50 eV, respectively. Along *b*-axis, the Ag/Cu electrodes have *n*-type Schottky barriers ($\Phi_L^{e,b}$) of 0.30/0.53 eV, respectively. The Pt/Ti/Pd/Au electrodes have *p*-type Schottky barriers ($\Phi_L^{h,b}$) of 0.40/0.41/0.42/0.54 eV, respectively. In other words, in *a* and *b* axis directions, the Ag and Au/Pd/Ti electrodes have Schottky contacts of the same polarity with GeSe (*n*- and *p*-type, respectively), while the Cu/Pt electrodes have Schottky contacts of totally opposite polarity. In the lateral interface, a build-in potential $\Delta\varphi$ exists between the electrodes and channel region and gives rise to the band bending, as shown in figure 7. Compared with the Cu/Ag/Au electrodes, the band bending in the channel is severe in the Pd/Pt/Ti electrodes, and the region of MIGS is broader. The contact type evaluated by the LDOS is in line with that by the TS.

The transport gap $E_g^{T,a}$ ($E_g^{T,b}$) define as:

$$E_g^{T,a} = \Phi_L^{e,a} + \Phi_L^{h,a} (E_g^{T,b} = \Phi_L^{e,b} + \Phi_L^{h,b}) \quad (4)$$

The values of $E_g^{T,a}$ are 1.07 (Au), 1.12 (Pt), 1.15 (Ti), 1.16 (Ag), 1.17 (Cu), and 1.24 (Pd) eV, and the values of $E_g^{T,b}$ are 0.88 (Ti), 1.04(Pd), 1.10(Cu), 1.11(Pt), 1.13(Ag), and 1.15 (Au) eV, respectively, which are all agreement with the intrinsic band gap of GeSe (1.15 eV).

The comparison of the lateral electron (hole) SBHs obtained at the WFA and transport simulation levels in the two axis directions (figure 8). These two methods have the same contact type in *b* axis, except for the Ti and Au electrodes, while the WFA and transport simulation give the opposite contact type in *a* axis, except for the Ag and Pd electrodes. The difference between the transport simulation in *a* and *b* axis directions and WFA is caused by the fact that the quantum transport simulation takes into account the effect between the metal electrodes and channel whereas the WFA ignores it. The interaction at the interface B often leads to the MIGS, which work as electrons reservoir and cause Fermi level pinning (FLP) preventing formation of a lateral ohmic contact.

The diagram of lateral electron SBH as a function of the metal work function in *a* and *b* axis of the GeSe FETs (figure 9(a)). The slope of the line fit to data, *S*, is known as pinning factor and represents the FLP level. $S = 0$ illustrates complete pinning and $S = 1$ illustrates no FLP. In *a* and *b* axis, the FLP factor is $S_a = -0.03$ and $S_b = 0.14$, respectively. But S_a makes little sense here due to the highly disperse data. The FLP factor in *b* axis is lower than the theoretical *S* values of ML BP (0.28) [8], ML blue phosphorene (0.42) [55], and ML arsenene (0.33) [41], suggesting stronger FLP at the lateral interface of GeSe. The stronger FLP effect in GeSe is due to more broad MIGS (figure 7). The GeSe/metal contact has a clearly strong FLP effect (figure 9(b)), and the Fermi level is pinned to a range of 0.64 eV in the band gap of the GeSe.

3.3. Improvement of the contact

The previous works have shown that using graphene electrodes or inserting graphene/BN between 2D semiconducting materials and bulk metal electrodes can reduce or even eliminate the SBH because the MIGS are strongly depressed by the Van der Waals contacts and Fermi level pinning is greatly weakened or absent [18, 40, 56]. To this end, we tried graphene and graphene-bulk metal hybrid electrodes. The binding energies are 0.26(graphene) and 0.34 eV (graphene-Cu), respectively, which are weaker than that of the other six

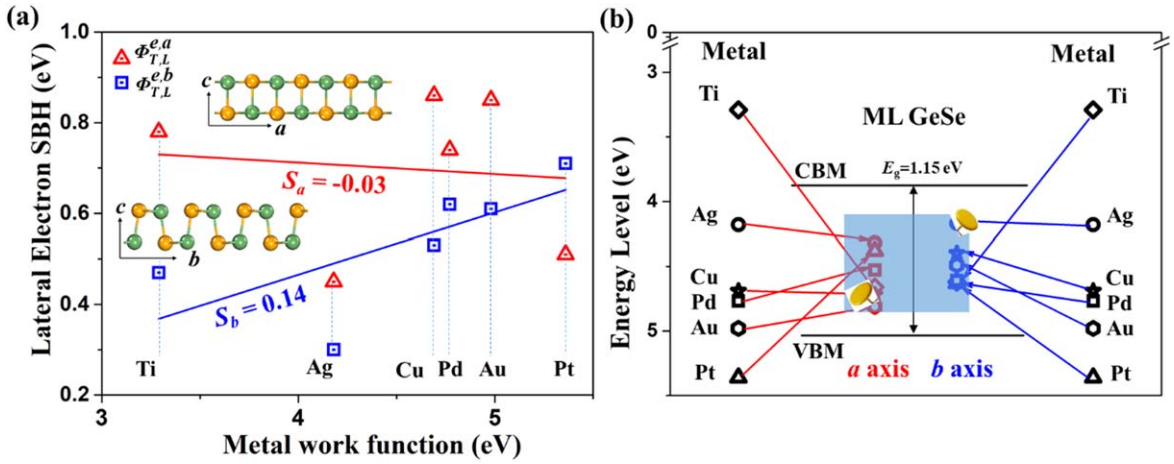

Figure 9. (a) The diagram of lateral electron SBH as a function of the metals (Ti(111), Ag(110), Cu(111), Pd(110), Au(110), and Pt(110)) work function in *a* axis and *b* axis for the GeSe FETs. *S* is the FLP factor. (b) Fermi level pinning (FLP) Diagram of the GeSe FETs.

common metal electrodes (except Ag), and weak chemical bonding is formed in those compound systems. Figure 10(a) shows the band structure of GeSe with graphene electrode. The band structure of GeSe contacted with graphene is same as the free standing GeSe because of a weak Van der Waals contacts and has a *p*-type vertical Schottky barrier of 0.17 eV. Figure 10 (b)/(c) show the LDOS projected on GeSe. In *a*-axis, there is a *p*-type lateral Schottky barriers of 0.1 eV (quasi-ohmic contact), which is consistent with the vertical Schottky barriers of 0.17 eV obtained from the band structure, and there is no Fermi-level pinning for absence of MIGS. In *b*-axis, remarkably, ohmic contact of *p*-type is formed. There are apparent MIGS near the VBM of GeSe in the lateral interface, and they accept electrons from both the electrode and channel, leading to a band bending and formation of an ohmic contact (as illustrated in figure S3). There is a 0.1 eV hole SBH far away from the interface in the electrode region, a result consistent with the band structure for the interfacial system.

Figure 10(d) shows the properties of electrons in the vertical interface of GeSe with graphene-Cu hybrid electrode. The dispersion relation of GeSe supported by graphene-Cu is consistent with the intrinsic GeSe, and a *p*-type Schottky barrier of 0.26 eV in the vertical interface. Figures 10(e)/(f) show the LDOS projected on the GeSe with graphene-Cu electrode. In the lateral interface of *a*-axis, a strong *p*-type lateral Schottky barrier of 0.04 eV averaged over the two electrodes, which treat as quasi-*p*-type ohmic contact. The apparent MIGS have connected the valence band of the channel, and the effective VBM is elevated. As a result, ohmic contact is formed at the left electrode. On the other hand, in *b*-axis, a weak *n*-type Schottky barrier of 0.47 eV averaged large electron SBH is formed because of apparent MIGS. It is clearly that 2D graphene electrode and insertion of graphene between GeSe and Cu electrode are superior to the six common metal electrodes. Hence, the GeSe FETs with 2D graphene electrode or graphene-Cu hybrid electrode should have a higher performance along *a*-axis direction.

4. Conclusion

In summary, we systematically study the contact properties between GeSe and different metal electrodes (Cu, Ag, Au, Ti, Pd, Pt, graphene, and graphene-Cu) in the transistor configuration by using DFT and quantum transport simulation. Anisotropic Schottky contacts are formed in the lateral interface of GeSe FETs. Along the *a*-axis of GeSe, the Ag and Pt electrodes have lateral *n*-type Schottky barriers of 0.45 and 0.51 eV, respectively, while the Au, Cu, Ti, and Pd electrodes have lateral *p*-type Schottky barriers of 0.22, 0.31, 0.37, and 0.50 eV, respectively. Along the *b*-axis of GeSe, the Ag and Cu electrodes have lateral *n*-type Schottky barriers of 0.30 and 0.53 eV, respectively, while the Pt, Ti, Pd and Au electrodes have lateral *p*-type Schottky barriers of 0.40, 0.41, 0.42, and 0.54 eV, respectively. The GeSe FETs have a strong Fermi level pinning factor of 0.14 in the *b*-axis. However, graphene electrodes have a highly desirable lateral *p*-type (quasi-*p*-type)) ohmic contact in the *b* (*a*)-axis direction. Upon insertion of graphene between GeSe and Cu, it has a quasi-*p*-type ohmic contact in the *a*-axis direction. Thus, GeSe FETs with graphene electrodes or with the insertion of graphene between GeSe and a Cu electrode could have higher performance.

Acknowledgments

The National Natural Science Foundation of China (No. 11704406/11674005) and Natural Science Basic Research Program of Shaanxi (Program No. 2019JM-355) support this work.

Conflicts of interest

None conflicts to declare.

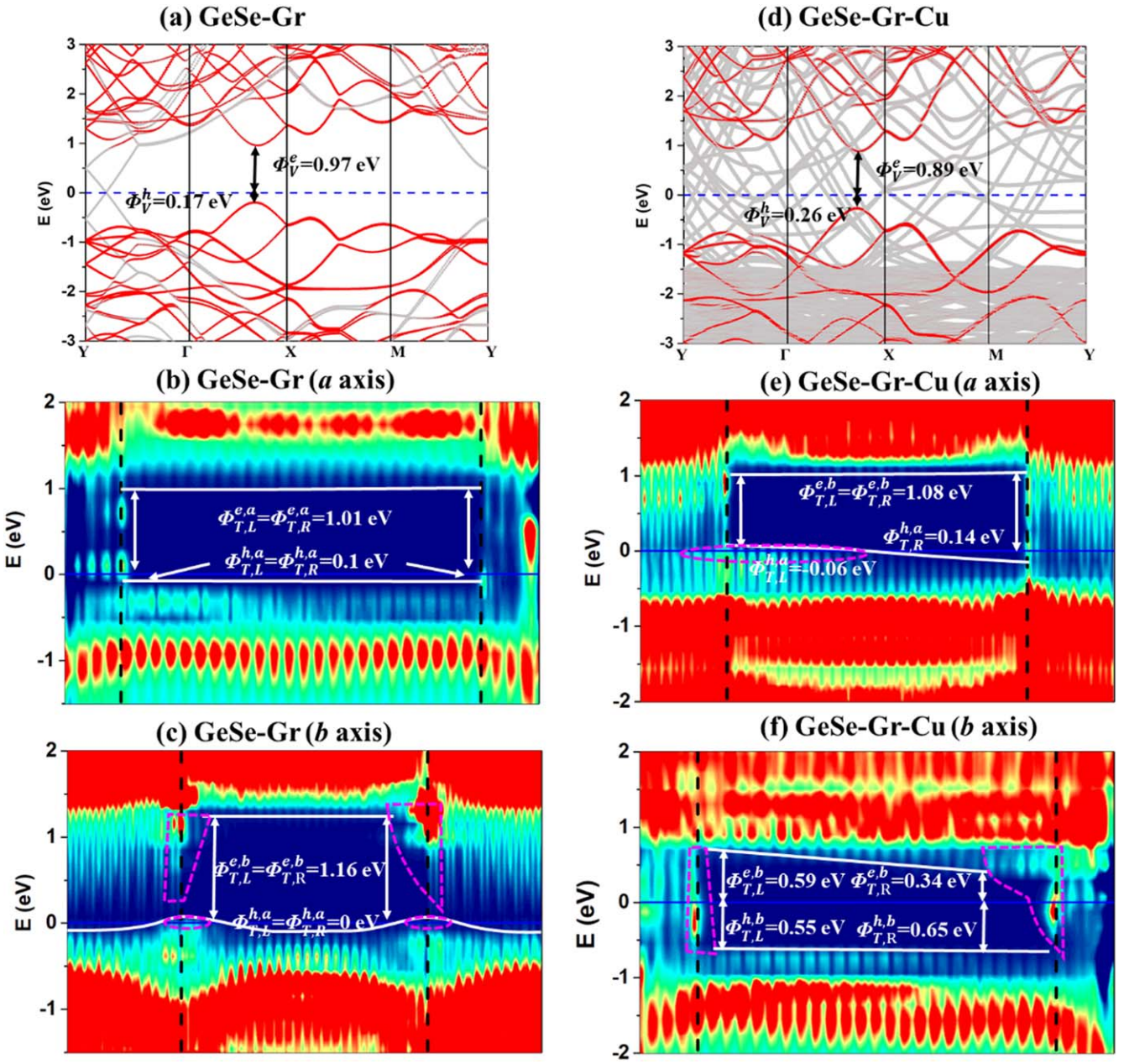

Figure 10. (a)/(d) Energy band structures of GeSe on the graphene and graphene-Cu, respectively. Gray dots correspond to the compound system. Red dots correspond to the states with valid contribution from GeSe, and the radii of the dots are proportional to the weight. The color coding of LDOS projected on the GeSe with graphene ((b)/(c)) and graphene-Cu electrode ((e)/(f)) under the zero-bias and zero-gate voltage, and the channel length is about 5 nm. Magenta lines surrounded area are the region with MIGS. The Fermi level is at zero energy. The upright black dashed lines are the interface of source (drain) and the channel. The conduction band and valence band profiles along the channel are given in white lines.

Supporting information available

Total electron density distributions of GeSe contacted with the metal electrodes; the energy band graph of the isolated GeSe/graphene electrode, the GeSe channel, and their combined system in *b* axis direction of the FETs.

ORCID iDs

Ying Guo https://orcid.org/0000-0002-3039-9425

References

[1] Desai S B *et al* 2016 MoS_2 transistors with 1-nanometer gate lengths *Science* **354** 99–102
[2] Reis F *et al* 2017 Bismuthene on a SiC substrate: a candidate for a hightemperature quantum spin Hall material *Science* **357** 287–90
[3] Li L *et al* 2014 Black phosphorus field-effect transistors *Nat. Nanotechnol.* **9** 372–7
[4] Wang Y *et al* 2018 Field-effect transistors made from solution-grown two-dimensional tellurene *Nat. Electronics* **1** 228–36

[5] Bandurin D A *et al* 2017 High electron mobility, quantum Hall effect and anomalous optical response in atomically thin InSe *Nat. Nanotechnol.* **12** 223–7

[6] Du Y *et al* 2017 One-dimensional van der waals material tellurium: Raman spectroscopy under strain and magneto-transport *Nano Lett.* **17** 3965–73

[7] Pizzi G, Gibertini M, Dib E, Marzari N, Iannaccone G and Fiori G 2016 Performance of arsenene and antimonene double-gate MOSFETs from first principles *Nat. Commun.* **7** 12585

[8] Pan Y *et al* 2016 Monolayer phosphorene–metal contacts *Chem. Mater.* **28** 2100–9

[9] Guo Y *et al* 2017 Monolayer bismuthene-metal contacts: a theoretical study *ACS Appl. Mater. Interfaces* **9** 23128–40

[10] Zhang X *et al* 2018 Three-layer phosphorene-metal interfaces *Nano Res.* **11** 707–21

[11] Wang Y *et al* 2015 Does p-type ohmic contact exist in WSe_2-metal interfaces? *Nanoscale* **8** 1179–91

[12] Wang Y *et al* 2017 Many-body effect, carrier mobility, and device performance of hexagonal arsenene and antimonene *Chem. Mater.* **29** 2191–201

[13] Chen P, Li N, Chen X, Ong W-J and Zhao X 2017 The rising star of 2D black phosphorus beyond graphene: synthesis, properties and electronic applications *2D Mater.* **5** 014002

[14] Yan J *et al* 2018 Monolayer tellurene–metal contacts *J. Mater. Chem.* C **6** 6153–63

[15] Ni Z *et al* 2016 Performance upper limit of sub-10 nm monolayer MoS_2 transistors *Adv. Electron. Mater.* **2** 1600191

[16] Kang J, Liu W, Sarkar D, Jena D and Banerjee K 2014 Computational study of metal contacts to monolayer transition-metal dichalcogenide semiconductors *Phys. Rev.* X **4** 031005

[17] Radisavljevic B, Radenovic A, Brivio J, Giacometti V and Kis A 2011 Single-layer MoS_2 transistors *Nat. Nanotechnol.* **6** 147–50

[18] Quhe R *et al* 2017 Can a black phosphorus Schottky barrier transistor be good enough? *ACS Appl. Mater. Interfaces* **9** 3959–66

[19] Avsar A *et al* 2015 Air-stable transport in graphene-contacted, fully encapsulated ultrathin black phosphorus-based field-effect transistors *ACS Nano* **9** 4138–45

[20] Fei R, Li W, Li J and Yang L 2015 Giant piezoelectricity of monolayer group IV monochalcogenides: SnSe, SnS, GeSe, and GeS *Appl. Phys. Lett.* **107** 173104

[21] Singh A K and Hennig R G 2014 Computational prediction of two-dimensional group-IV mono-chalcogenides *Appl. Phys. Lett.* **105** 042103

[22] Li L *et al* 2013 Single-layer single-crystalline SnSe nanosheets *J. Am. Chem. Soc.* **135** 1213–6

[23] Brent J R *et al* 2015 Tin(II) sulfide (SnS) nanosheets by liquid-phase exfoliation of herzenbergite: IV–VI main group two-dimensional atomic crystals *J. Am. Chem. Soc.* **137** 12689–96

[24] Xu L, Yang M, Wang S J and Feng Y P 2017 Electronic and optical properties of the monolayer group-IV monochalcogenides MX (M=Ge,Sn; X=S,Se,Te) *Phys. Rev.* B **95** 235434

[25] Ji Y, Yang M, Dong H, Wang L, Hou T and Li Y 2017 Monolayer group IVA monochalcogenides as potential and efficient catalysts for the oxygen reduction reaction from first-principles calculations *J. Mater. Chem.* A **5** 1734–41

[26] Zhou Y 2016 MX (M=Ge, Sn; X=S, Se) sheets: theoretical prediction of new promising electrode materials for Li ion batteries *J. Mater. Chem.* A **4** 10906–13

[27] Liu S-C *et al* 2017 Investigation of physical and electronic properties of GeSe for photovoltaic applications *Adv. Electron Mater.* **3** 1700141

[28] Zhao H *et al* 2018 Band structure and photoelectric characterization of GeSe monolayers *Adv. Funct. Mater.* **28** 1704855

[29] Hu Y, Zhang S, Sun S, Xie M, Cai B and Zeng H 2015 GeSe monolayer semiconductor with tunable direct band gap and small carrier effective mass *Appl. Phys. Lett.* **107** 122107

[30] Vaughn D D II, Romesh J P, Hickner M A and Schaak R E 2010 Single-crystal colloidal nanosheets of GeS and GeSe *J. Am. Chem. Soc.* **132** 15170–2

[31] Lv X, Wei W, Mu C, Huang B and Dai Y 2018 Two-dimensional GeSe for high performance thin-film solar cells *J. Mater. Chem.* A **6** 5032–9

[32] Xue D J *et al* 2017 GeSe thin-film solar cells fabricated by self-regulated rapid thermal sublimation *J. Am. Chem. Soc.* **139** 958–65

[33] Xia C, Du J, Xiong W, Jia Y, Wei Z and Li J 2017 A type-II GeSe/SnS heterobilayer with a suitable direct gap, superior optical absorption and broad spectrum for photovoltaic applications *J. Mater. Chem.* A **5** 13400–10

[34] Mukherjee B, Cai Y, Tan H R, Feng Y P, Tok E S and Sow C H 2013 NIR Schottky photodetectors based on individual single-crystalline GeSe nanosheet *ACS Appl. Mater. Interfaces* **5** 9594–604

[35] Xue D J, Tan J, Hu J S, Hu W, Guo Y G and Wan L J 2012 Anisotropic photoresponse properties of single micrometer-sized GeSe nanosheet *Adv. Mater.* **24** 4528–33

[36] Lv X, Wei W, Sun Q, Li F, Huang B and Dai Y 2017 Two-dimensional germanium monochalcogenides for photocatalytic water splitting with high carrier mobility *Appl. Catal.* B **217** 275–84

[37] Pan Y *et al* 2017 Schottky barriers in bilayer phosphorene transistors *ACS Appl. Mater. Interfaces* **9** 12694–705

[38] Gao J, Nandi D and Gupta M 2018 Density functional theory —projected local density of states—based estimation of Schottky barrier for monolayer MoS_2 *J. Appl. Phys.* **124** 014502

[39] Allain A, Kang J, Banerjee K and Kis A 2015 Electrical contacts to two-dimensional semiconductors *Nat. Mater.* **14** 1195–205

[40] Liu Y, Weiss N O, Duan X, Cheng H-C, Huang Y and Duan X 2016 Van der Waals heterostructures and devices *Nat. Rev. Mater.* **1** 16042

[41] Wang Y *et al* 2017 Electrical contacts in monolayer arsenene devices *ACS Appl. Mater. Interfaces* **9** 29273–84

[42] de Oliveira I S S and Longuinhos R 2016 Effects of oxygen contamination on monolayer GeSe: a computational study *Phys. Rev.* B **94** 035440

[43] Kresse G and Joubert D 1999 From ultrasoft pseudopotentials to the projector augmented-wave method *Phys. Rev.* B **59** 1758–75

[44] Kresse G and Furthmüller J 1996 Efficient iterative schemes for Ab initio total-energy calculations using a plane-wave basis set *Phys. Rev.* B **54** 11169–86

[45] Grimme S, Antony J, Ehrlich S and Krieg H 2010 A consistent and accurate *ab initio* parametrization of density functional dispersion correction (DFT-D) for the 94 elements H-Pu *J. Chem. Phys.* **132** 154104

[46] Grimme S, Ehrlich S and Goerigk L 2011 Effect of the damping function in dispersion corrected density functional theory *J. Comput. Chem.* **32** 1456–65

[47] Neugebauer J and Scheffler M 1992 Adsorbate-substrate and adsorbate-adsorbate interactions of Na and K adlayers on Al(111) *Phys. Rev.* B **46** 16067–80

[48] Pan Y *et al* 2017 Schottky barriers in bilayer phosphorene transistors *Acs Appl. Mater. Inter.* **9** 12694–705

[49] Pan Y Y *et al* 2016 Monolayer phosphorene-metal contacts *Chem. Mater.* **28** 2100–9

[50] Movva H C *et al* 2015 High-mobility holes in dual-gated WSe_2 field-effect transistors *ACS Nano* **9** 10402–10

[51] Das S, Chen H Y, Penumatcha A V and Appenzeller J 2013 High performance multilayer MoS_2 transistors with scandium contacts *Nano Lett.* **13** 100–5
[52] Liu Y *et al* 2018 Approaching the Schottky–Mott limit in van der Waals metal–semiconductor Junctions *Nature* **557** 696–700
[53] Kaushik N *et al* 2014 Schottky barrier heights for Au and Pd contacts to MoS_2 *Appl. Phys. Lett.* **105** 113505
[54] Kim C *et al* 2017 Fermi level pinning at electrical metal contacts of monolayer molybdenum dichalcogenides *ACS Nano* **11** 1588–96
[55] Li J *et al* 2018 Electrical contacts in monolayer blue phosphorene devices *Nano Res.* **11** 1834–49
[56] Liu Y, Paul S and Wei S-H 2016 Van der Waals metal-semiconductor junction weak fermi level pinning enables effective tuning of Schotty barrier *Sci. Adv.* **2** e1600069